

Multiscale Modelling of the Laser Beam Welding Part II Microscopic Scale

H.-J. Diepers^a, I. Steinbach^a, V. Plochikhine^b, H.-W. Zoch^b, V.A. Karkhin^c, H.-J. Pesch^c

a. ACCESS e.V., Aachen,

b. Neue Materialien Bayreuth, Bayreuth

c. Institute for Mathematics in Engineering Sciences, Uni Bayreuth

The process of the laser beam welding of Al-Si alloys is simulated on the different length scales. This second part of the work reconstructs the microstructure and microsegregation by direct simulation using the phase field method. In the typical parameter window $d/dt T = 1000\text{K/s} - 12000\text{K/s}$ and $\nabla T = 500-4000\text{K/cm}$ systematic investigations by 2D- simulations were carried out in order to describe the morphology diagram. Double-dendritic transitions are observed and the primary spacing is evaluated as function of solidification conditions. Differences in simulation results are discussed for the cases of binary and ternary alloys, two and three dimensional simulations, and different models of crystal anisotropy. The results are compared with the measured microstructure in the weld pool.

1 Introduction

Heat treatments of surfaces with high energy sources lead to specific melting and solidification conditions with cooling rates $d/dt T \approx 10^4\text{K/s}$. The correspondent deviations from the thermodynamic equilibrium lead to specific microstructure formation implying specific material properties. The lack of basic knowledge hinders often technical applications. The physics of short time metallurgy becomes manifest by the heat distribution down to atomistic attachment processes at microscopic scale. So the modeling of the laser remelting process on macroscopic, mesoscopic and microscopic scale is necessary to understand the fundamental processes. In this contribution, we investigate the laser treatment of Al-Si alloys on different length scales. Al-Si alloys are of technical interest in airplane and automobile construction. Although rapid solidification is a topic of theoretical research for many years [1,2] many basic questions are open. Classical microstructure models for solidification fail, as they neglect atomistic attachment kinetics and non equilibrium interfacial solute partitioning. Also primary spacing models based on numerical calculations [3] are in doubt [4], as they reduced the problem on unit cells in 2D and neglect atomistic anisotropic dependencies. Some of those theoretical discussions are linked to the present applications of laser beam welding for Al-Si alloys by the direct numerical simulation of microstructural evolution based on phase-field modelling. First the simulation model and basic physics are presented. Then processing conditions, material data and assumptions, which are used for the direct simulation are specified. The results based on this model concern 2D and 3D simulations. The 2D cases focus on the morphological changes and the evolving primary spacing due to processing parameters. Further discussion will be given to the influence of different anisotropy models and exemplary a third alloying element (Cu) processed Al material AC120. Exemplary 3D calculations extend the comparability to experimentally measured microstructures.

2 The phase-field model and process parameters

The physics of solidification is determined by the minimization of free energy during phase change, which goes along with by thermal, solutal and capillar undercooling. The subsequent (equilibrium) condition must be extended by kinetic contributions for rapid solidification conditions [5], resulting in the extended Gibbs Thomson relation

$$v = \mu(\mathbf{Q}) [T_m - T + m_l c_l - \Gamma(\mathbf{Q}) \kappa] \quad (1)$$

, where μ describes the attachment kinetics, κ is the interface curvature Γ is the GibbsThomson coefficient. Solid Metals are anisotropic, so μ and Γ depend in their own way on Θ = angle between crystal orientation and growth direction. The influence of solute on melting temperatur is expressed by the liquidus slope in a linearized phase diagram (see Fig1). The material and heat transport at the interface is affected by the relase of latent heat and solute redistribution. As the thermal diffusivity is 3 orders of magnitude higher than the solutal one, the temperature field can be regarded usually as linear against the solutal diffusion length.

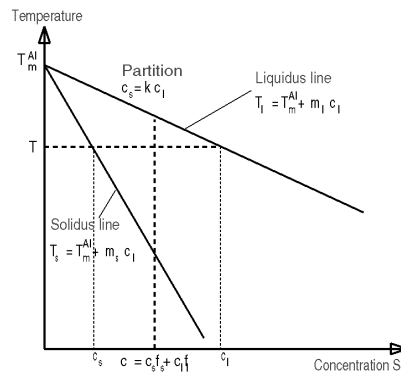


Figure 1. Scheme of a linear phase-diagram

2.1 Phase-field model

The phase field equation (2) describes the propagation of solid phase indicated by the phase-field parameter ϕ changing from liquid ($\phi=0$) to solid ($\phi=1$).

$$d/dt \mathbf{f} = \mathbf{mG} [\tilde{\mathbf{N}}^2 \mathbf{f} + 36/d^2 \mathbf{f}(1-\mathbf{f})(1-2\mathbf{f})] + (T_m - T + m_l \langle c_l \rangle) 140/d \mathbf{f}^3 (1-\mathbf{f})^3 \quad (2)$$

This equation evokes a continuous phase transition within a thin layer of thickness δ (s. Fig2), therewith propagating due to the extended Gibbs-Thomson equation(1). For details see [6, 7]. The presented form is a special case of the multiphase-multicomponent phase field model given in [8]. In the multicomponent case (see section 3.4) the term $m_l c_l$ is replaced by the sum of constituents/ their solutal undercoolings $\rightarrow \sum_i m_i^l c_i^l$. Therefore a linearized liquidus plane is assumed.

The coupled concentration profile of a solutal component c^i is modeled by

$$d/dt c^i = \tilde{\mathbf{N}} D^i(\mathbf{f}) [\tilde{\mathbf{N}} c^i - (1-k^i) c_l^i \tilde{\mathbf{N}} \mathbf{f}] \quad , \quad c = c_l^i (1-\mathbf{f} + k^i \mathbf{f}) \quad (3)$$

describing diffusion in liquid (solid diffusion here is neglected) by phase dependend diffusivity $D^i(\mathbf{f})$. As described in [9] the solute partitioning depends on the solidification velocity and is reduced from its equilibrium value k by solute trapping at high velocities. For numerical stability reasons some modifications are introduced in the original model [6,7,8]: In eq. (2) the concentra-

tion is taken as interfacial average $\langle c_i \rangle$. The term $6\phi(1-\phi)$ is replaced by $140\phi^3(1-\phi)^3$. A moving frame algorithm has been introduced in order to track the interface within a constant undercooling range for the temperature field cooling down. Details are described in [10].

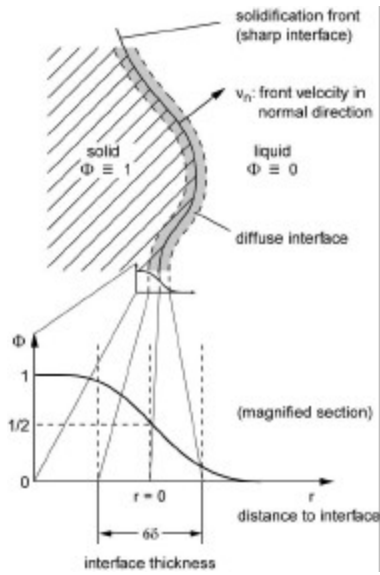


Figure 2. Scheme Phase-field approach. The front propagation is projected on a diffuse interface of thickness δ

Table 1 Material and numerical parameters

Melting temperature	T_m^0	933.6 K
Silicon liquidus slope	m_l^{Si}	-6 K/%
Silicon partition coefficient	k^{Si}	0.13
Copper liquidus-slope	m_l^{Cu}	-2.6 K/%
Silicon partition coefficient	k^{Cu}	0.14
Diffusivity (for Si and Cu)	D_l	$3 \cdot 10^{-9} \text{ m}^2/\text{s}$
Gibbs-Thomson coefficient	Γ	$2.4 \cdot 10^{-7} \text{ mK}$
Attachment kinetics	μ	0.12 m/sK
Degree of Anisotropy	α	See case, else 7.5 %
PFM interface width	δ	0.3 μm
Numerical grid spacing	Δx	0.1 μm
time resolution	Δt	0.05 μs

2.2 Material and process parameters for Laser welding Al-Si-Cu

The processed alloy material AC120 (AlSi1.2Fe0.3Mg0.4Cu0.13) was usually modeled by its main constituent (AlSi1.2). Some ternary simulations with copper were performed also (s. Section. 3.3.). Most of the AlSi physical properties are described in [1] and the actually used numerical data are summarized in Table 1. The crystal anisotropic behavior of metals may be assumed to be cubic and can be modeled [2] in 2D with four-fold anisotropic surface tension or attachment kinetics:

$$\sigma(\Theta) = \sigma_0 [1 + \gamma \cos(4\Theta)] \quad \text{equivalent} \quad \Gamma(\Theta) = \Gamma_0 [1 - \alpha \cos(4\Theta)] \quad \text{with } \alpha=15 \gamma \quad (4)$$

$$\mu(\Theta) = \mu_0 [1 + \beta \cos(4\Theta)] \quad (5)$$

The angular dependence is sketched in Fig 3 together with a correspondent axisymmetric 3D formulation. α and β describe the strengths of anisotropy, typically between 7% and 75%. Unfortunately no reliable data are known especially for β , so that several models for anisotropy are tested in section (4.3). Most simulations are done with weak anisotropy (7.5%). From the macroscopic modeling the mesoscopic solidification conditions determined to lie in the following range: $v = 1\text{-}3 \text{ cm/s}$; $\text{grad } T = 500\text{-}4000 \text{ K/cm}$, which corresponds to cooling rates from 500 to 12000 K/s.

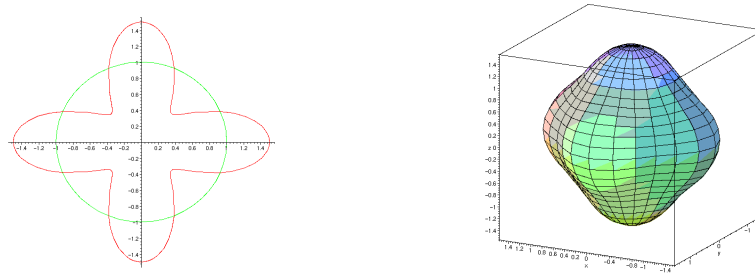


Figure 3. Anisotropy of surface tension/ attachment kinetics in 2D and 3D

3 2-D Simulations

Fig. 4 shows a time sequence in the calculation domain ($40 \times 20 \mu\text{m}^2$), which was moved with the velocity of the temperature field, where $v = -d/dt T / G$. First primary trunks evolve from three initially setted nuclei. The asymmetry prescribed thereby is used to see influences of starting conditions on the evolving microstructure. So one initial side branch fills rapidly the right side of the domain. Ternary arms then form a dense array of future primary trunks. All this finally builds an array of stem like structures without sidebranches, as observed in short time processed experimental micrographs [17]. Typical selection behaviour occurs, when the tips slow down to steady state velocities due to the imposed cooling rate. After 10^{-3} s a stable primary spacing of $\lambda=2.5 \mu\text{m}$ is formed. In the next paragraph only the final states of the simulations are shown.

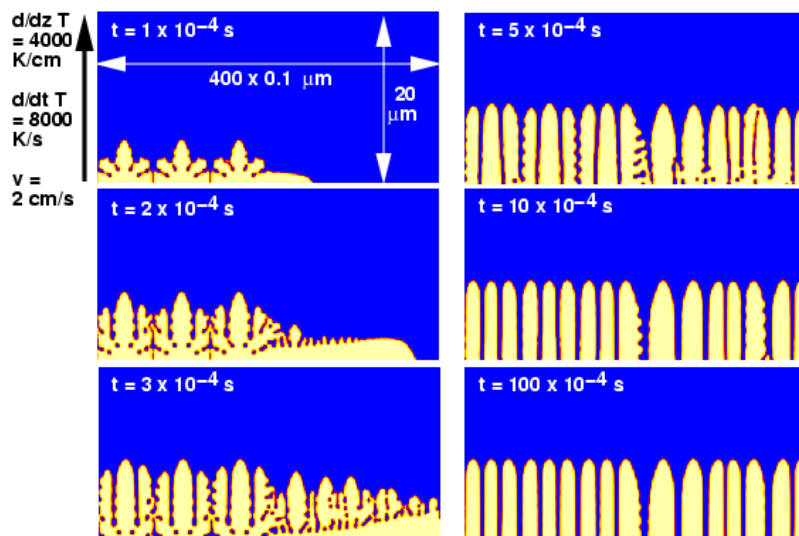


Figure 4. Time evolution of microstructure in AlSi1.2 for laser processing conditions ($v=2\text{cm/s}$, $G = 4000 \text{ K/cm}$). Color represents the phase field (black = liquid, white= solid). The crystal anisotropy in surface tension is $\alpha= 7.5\%$.

3.1 Influence of processing parameters

The simulations as in Fig 4 were repeated for different cooling rates and temperature gradients. The results (at steady state/ $t=10^{-2}$ s) are presented in Figure 5, here in terms of silicon content. In addition to the morphology the different solvabilities of Si in solid/liquid and the interdendritic

solute diffusion can be seen. Quite interesting is the manifoldness of observed morphologies. For the lower velocities the dendrites have quite unstable tip formations, accompanied by side branching. They coexist with doublon like structures, which grow pairwise, separated by a small solute channel. Doublons occur for low anisotropies or for high undercoolings (Detailed experimental and theoretical descriptions of doublons are given in [11], [12]). By interpreting this results we have to keep in mind, that the applied anisotropy was chosen quite weak. Changes due to different anisotropy models are demonstrated in the next section. For velocities $v > 2$ cm/s sidebranches are absent and the evolved microstructures are directed to the crystal orientation/ the temperature gradient. Qualitative tendencies are observable for the primary spacing λ : The spacing reduces with increasing velocity and with increasing temperature gradient. It should be recognized, that the primary spacing is not unique and especially for gradients $G < 2000$ K/cm the spacing is asymmetric: dendrites formed from the initial seeds (left side) build bigger spacings than those resulting from the dense ternary arm array (see Figure 4 for the formation history). The history dependence of spacings is well known from experiments [14] and simulations [16].

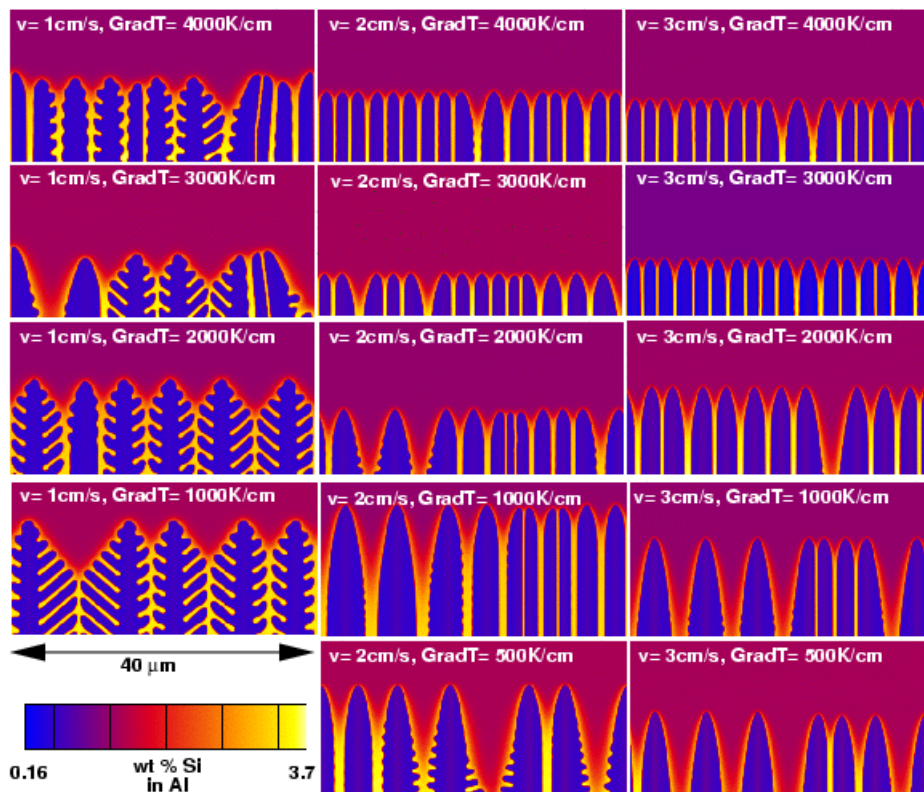


Figure 5. Microstructure and microsegregation for different processing parameters. Other parameters are the same as in Figure 4

3.2 Evaluation of primary spacings

Classical theories on primary spacing λ as given in [15] or [1] predict dependencies as $\lambda \sim v^{-1/4} G^{-1/2}$. In the simulations values from 2 – 8 μm are reached. The evaluation of λ in the simulations against the cooling rate v is shown in Figure 6/ left. The broad distribution range of individual spacings is indicated by errorbars for $G = 4000$ K/cm. Two analytical lines are added here to compare the simulation results with classical spacing predictions $\lambda \sim v^{-1/4}$. The exponent $-1/4$ is more

valid in the range $v > 1.5$ cm/s, where in contrast in the regime $v \sim 1.5$ cm/s the spacing fits better to $\lambda \sim v^{-1}$. This is reasonable because here the morphology type changes the spacing distribution (see Fig 5). Log-log plotting λ against the temperature gradient G (Fig 6/ right) the results fit to the classical dependency $\lambda \sim G^{-1/2}$ (for those cases, where the morphology changes are irrelevant).

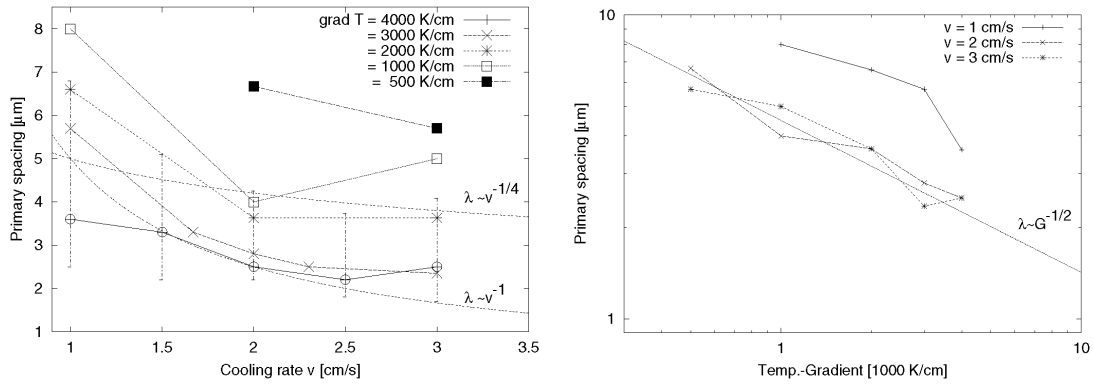


Figure 6. Primary spacings against cooling rate v and temperature gradient G

3.3 Influence of anisotropy

The morphologies in Fig 5 (for $v=1$ cm/s $G=4000$ K/cm) were subject of the anisotropy changes in the numerical model due to eq (4) and (5). The correspondent morphologies are shown in Figure 8. A stronger anisotropy in surface tension (left) reduces the

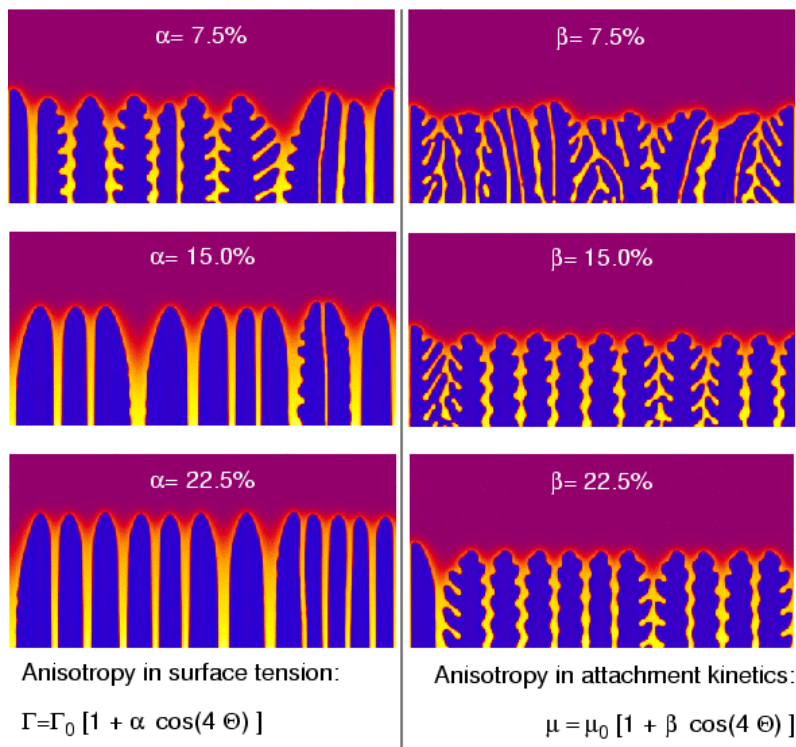


Figure 7. Different anisotropies in surface tension (left) or attachment kinetics (right).

presence of doublons and stabilizes the tip formation. The primary spacing is affected by the anisotropy influence on microstructure. Applying finite anisotropy in attachment kinetics (right) results in more seaweed like structures (unoriented doublons) for weak anisotropy. For for stronger

kinetic anisotropies the doublons vanish, but unstable tip formation remains present. It seems, that under applied conditions the anisotropy of surface tension is more significant than that of attachment kinetics. As it is well known, that the anisotropy affects seriously the tip selection and growth morphology [2,12,13], also influences of anisotropy on primary spacing should be investigated by systematic continuation of direct simulations to extend the model of [3].

3.4 Influence of a ternary component

Some calculations were performed with AISi1.2Cu0.13 to study influences of the ternary component Cu. Figure 7 faces binary and ternary calculations for $G=4000\text{K/cm}$, $v=1\text{cm/s}$ $v=2\text{cm/s}$). For both applied cooling rates, the ternary interface position in the temperature gradient and therewith the tip undercooling is different from AISi1.2. At $v=1\text{cm/s}$ the morphology type changes little, when by adding of Cu the doublons vanish. In both cases, the relevance of the low ternary alloying is too small to change the primary spacing λ .

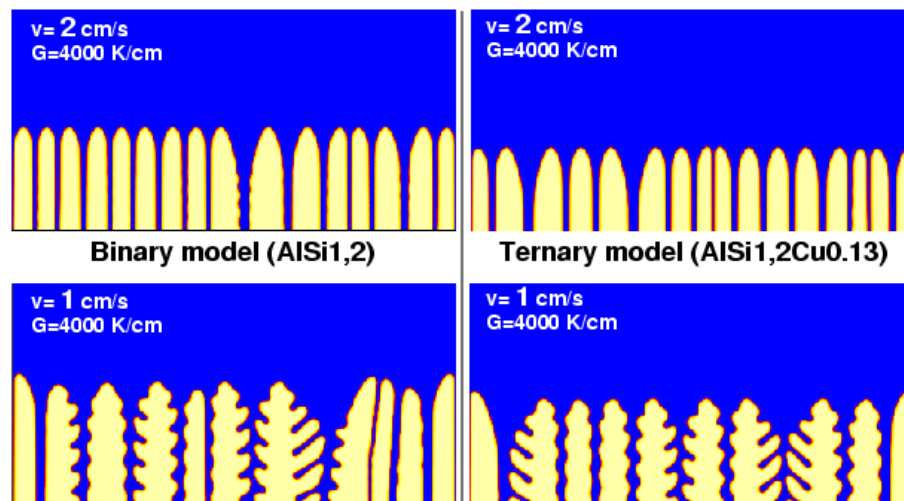


Figure 8. Microstructure for binary (left) and ternary alloy (right).

4 3-D Simulations

Exemplary 3-D simulations have been performed. Due to restrictions of computer memory and time the domain is chosen smaller in x direction than in 2D. The preferred crystal directions were set in direction to the x,y and z-axis. Figure 9 shows a calculation again for $v=2\text{cm/s}$ and $G=4000\text{K/cm}$. The anisotropy ($\beta=7.5\%$) is implied in the attachment kinetics. The stemlike dendrites build in contrast to 2D cases not a parabolic shape, but 4 fold swellings in x and y-direction, as predicted by theorie [13]. The time sequence is in principal similar to the 2-D evolution in fig. 4. After selection we observe nearly steady state conditions at $t=10^{-4}\text{s}$. The primary spacing $\lambda\sim 2.1\mu\text{m}$ is a bit smaller, but comparable to the 2D case ($2.5\mu\text{m}$).

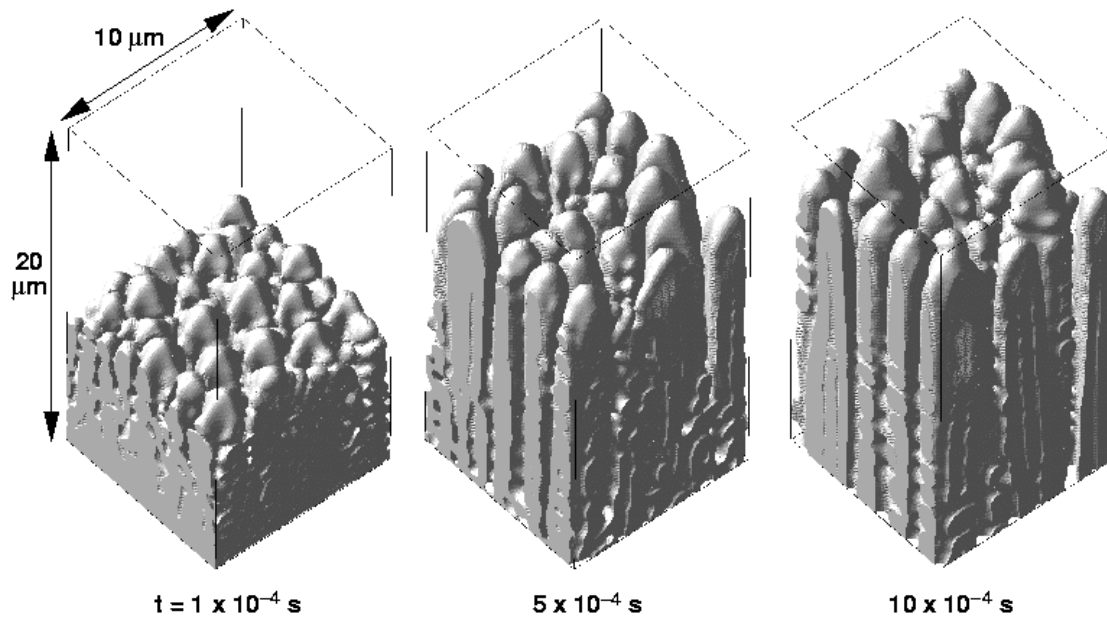


Figure 9. Three dimensional simulations for $v= 2\text{cm/s}$, $G = 4000\text{K/cm}$

4.1 Parameter variations in 3D

As in 2D, effects of changing anisotropy and processing parameters have been tested exemplarily. Figure 10 shows comparisons from the top view. For reduced velocity ($v=1\text{cm/s}$) the primary spacings coarsen to $\lambda \sim 2.4 \mu\text{m}$ (from $\lambda \sim 2.1 \mu\text{m}$ at $v=2\text{cm/s}$) in the simulations with anisotropic kinetics. The morphology change known from 2D at the low speed is not apparent. A comparable change is present only, if the surface tension is assumed to be anisotropic. The array is unstable here and tip splitting occurs at both cooling rates. Further discussion will be given elsewhere.

5 Comparisons with experiments.

Figure 11 shows the microstructure of the specimen AC120, which was processed with a speed of 2.5 cm/s . At the bottom and top-position of the welding track the microstructures differ by orientation and by primary spacing: For the spacing λ we measured average values $\lambda_{\text{top}} = 2 \mu\text{m}$ and $\lambda_{\text{bottom}} = 3 \mu\text{m}$ within a modulation of about $1.5 \mu\text{m}$. This range fits very good to the simulation results (3D is still better than 2D). The smaller spacings at top, which are due to locally higher local cooling rates, are reflected by the simulation tendencies of λ against v (see Fig 6).

6 Conclusions

A phase field model has been applied to model directly the microstructure evolution during solidification for typical conditions for laser beam welding. These simulations connect to the foregoing macroscopic and mesoscopic simulation models by use of the estimated cooling conditions. The resulting microstructures in 2D and 3D look quite realistic against experimental micrographs. The simulated microstructures depend remarkably on the processing parameters (cooling rate, Temperature gradient). Morphology changes are observed, which also depend crucially on the applied crystal anisotropy model. Classical primary spacing models fail in regimes of morphological chan-

ges. In regimes of stable morphologies they seem to work well. Exemplary simulations in 3D allow for new insight in microstructure formation. The present investigations are an encouraging start for more detailed examinations.

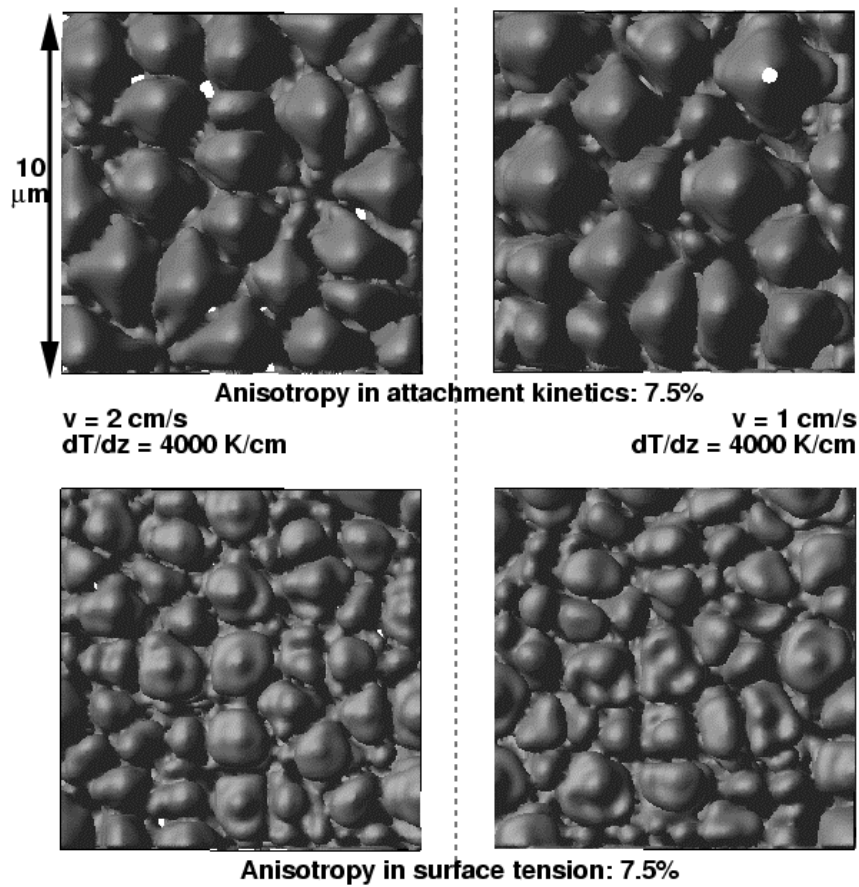


Figure 10. Influence of processing and anisotropy parameters in 3D

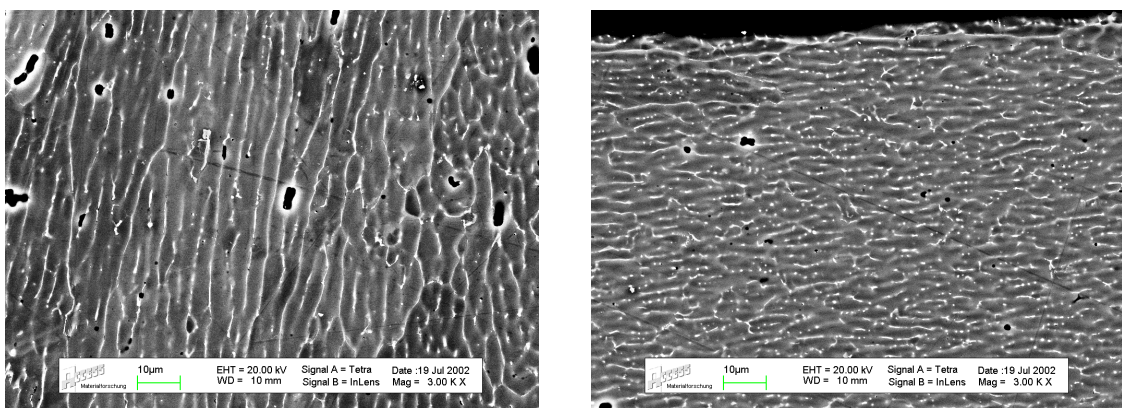


Figure 11. Experimental microstructure /length section at bottom (left) and top (right) of the welding track ($v=2.5\text{cm/s}$ welding speed and $P = 1.7\text{ kW}$).

References

- [1] W. Kurz, D.J. Fisher, "Fundamentals of Solidification" Transtech publications Aedermannsdorf, Switzerland (1992)

- [2] H. Müller Krumbhaar, W. Kurz "Solidification", in Materials Science and Technology, Eds. R.W. Cahn, P. Haasen, E.J. Kramer, Vol 5, Weinheim (1991)
- [3] S. Lu and J.D.Hunt "A Numerical Analysis of Dendritic and Cellular Array Growth: The Spacing Adjustment Mechanisms" J. Crystal Growth 123, pp 17-34 (1992)
- [4] W.J. Boettinger, S.R. Coriell, A.L. Greer, A. Karma, W. Kurz, M. Rappaz, R. Trivedi: "Solidification Microstructures: Recent Developments, Future Directions" W.J. Boettinger, S.R. Coriell, A.L. Greer, A. Karma, W. Kurz, M. Rappaz and R. Trivedi, Acta mater. 48, pp.43-70 (2000)
- [5] R. Trivedi, W. Kurz Solidification "Microstructures: A conceptual approach (Overview Nr. 10), Acta metal mater. Vol 42, No 1, pp 13-23, 1994
- [6] H. Diepers, C. Beckermann, I. Steinbach "A phase-field Method for Alloy Solidification with Convection" Solidification Processing 1997, Eds. J. Beech and H. Jones, University of Sheffield, UK 1997, pp. 426 (1997)
- [7] C.Beckermann, H.Diepers, I.Steinbach, A.Karma, X.Tong "Modeling Melt Convection in Phase-field Simulations of Solidification", J. Comp.Phys154,pp468-496 (1999)
- [8] J. Taden, B. Nestler, H. Diepers, I. Steinbach "The Multiphase-Field Model with an Integrated Concept for Modeling Solute Diffusion", Physica D 115, pp73-86 (1998)
- [9] S.G. Kim, W.T. Kim, T. Suzuki "Phase-field Model for Binary Alloys", Phys Rev. E, Vol 60,6, pp 7186 -7197 (1999)
- [10] H. Diepers: "Simulation des Primärabstandes gerichtet erstarrter Dendriten mit der Phasenfeldmethode" Diss. am Gießereinstitut der RWTH Aachen (to be published).
- [11] S. Akamatsu, G.Faivre and T.Ihle "Symmetry broken Double Fingers and Seaweed Patterns in Thin Film Directional Solidification of a Nonfaceted cubic Crystal", Phys Rev. E, Vol. 51/5, S 4751-4773 (1995)
- [12] E. Brener , H. Müller Krumbhaar, D. Tempkin, T. Abel "Structure Formation in Diffusional Growth and Dewetting" Solid State Ionics 131, pp. 23-33, (2000)
- [13] M. Ben Amar, E. Brener "Theory of pattern selection in three dimensional nonaxisymmetric dendritic growth" Phys. Rev. Let. 71,4 pp 589-592
- [14] X. Lin, Huang, J. Feng, T. Li, Y. Zhou "History dependent Selection of Primary cellular/Dendritic spacing during unidirectional solidification in Aluminium Alloys", Acta mater. vol 47, pp 3271-3280
- [15] J. D. Hunt "Cellular and primary dendrite spacings" solidification and casting of metals, Book 192, pp. 3-9, The metals society London (1979).
- [16] H. Diepers, D.Ma, I.Steinbach: "History effects during the selection of primary dendrite spacing. Comparison of phase-field simulations with experimental observations", J. Cryst. Growth 237-239, pp 149-153 (2002)